Gemini/GMOS Integral Field Unit stellar kinematics of the nuclear region of six nearby active galaxies

F. K. B. Barbosa,[1]⋆ T. Storchi-Bergmann,[1] R. Cid Fernandes,[2] Cláudia Winge[3] and H. Schmitt[4,5]

[1]*Instituto de Física – UFRGS, Caixa Postal 15051, CEP 91501-970, Porto Alegre, RS, Brazil*
[2]*Departamento de Física, CFM – UFSC, Campus Universitário – Trindade, CP 476, CEP 88040-900, Florianópolis, SC, Brazil*
[3]*Gemini Observatory, Casilla 603, La Serena, Chile*
[4]*Remote Sensing Division, Code 7210, Naval Research Laboratory, 4555 Overlook Avenue, SW, Washington, DC 20375, USA*
[5]*Interferometric Inc., 13454 Sunrise Valley, Suite 240, Herndon, VA 20171, USA*

ABSTRACT

We present 2D mapping of the stellar velocity field within the inner 5 arcsec of six nearby active galaxies, using spectra obtained with the Integral Field Unit (IFU) of the Gemini Multi-Object Spectrograph instrument at the Gemini North telescope. The sampling of the observations is 0.2 arcsec, corresponding at the galaxies to spatial extents ranging from 10 to 30 pc. The spatial resolution range from 20 to about 180 pc, and the observed field of view covers a few hundred parsecs around the nuclei. The Ca II triplet absorption features at $\approx$8500 Å were used to measure the stellar radial velocities and velocity dispersions. The radial velocity fields are dominated by rotation in all galaxies. A simple kinematical model assuming a purely rotating system with circular orbits in a plane was fitted to the radial velocity data. The turnover of the rotation curve is at only $\approx$50 pc for NGC 4051 and between 200 and 700 pc for the other five galaxies. The velocity dispersion (σ) maps show the largest values ($100 \geqslant \sigma \geqslant 150\,\mathrm{km\,s^{-1}}$) at the centre. In the cases of NGC 2273 and 3227, there is a decrease to $\sigma \approx 70$–$80\,\mathrm{km\,s^{-1}}$ at $\approx$200–300 pc from the nucleus, delineating partial rings of low-σ values. A similar broken ring seems to be present at $\approx$400 pc from the nucleus also in NGC 4593. We interpret these low-σ rings as traces of recently formed stars that partially keep the cold kinematics of the original gas from which they have formed. In NGC 3516 there is a decrease of σ outwards with the steepest gradient observed along the direction of the galaxy major axis, where σ reaches $\approx$80–90 $\mathrm{km\,s^{-1}}$ at $\approx$400 pc from the nucleus.

The main novelty of the present work is the unprecedented spatial resolution reached by a 2D study of stellar kinematics of Seyfert galaxies using an IFU. The few similar IFU studies available in the literature for Seyfert galaxies have a much poorer spatial resolution and/or are restricted to the study of emission-line kinematics.

Key words: stellar dynamics – galaxies: active – galaxies: kinematics and dynamics – galaxies: nuclei – galaxies: Seyfert – galaxies: starburst.

1 INTRODUCTION

It is now widely accepted that active galactic nuclei (AGN) are powered by the accretion of material on to a central supermassive black hole (SMBH). The present paradigm for the evolution of galaxies is that all galaxies which form bulges also form a SMBH at their centres (Ferrarese & Merritt 2000; Gebhardt et al. 2000). In this sce-

nario, the active galaxies are those in which the SMBH is presently accreting material from its surroundings.

A problem still under investigation is the mechanisms by which the material is dragged to the nuclear regions to feed the AGN, as the galactic gas must lose almost all of its angular momentum in order to reach the central few parsecs. Signatures that such feeding is occurring include the frequent occurrence of recent star formation around AGN, which implies the existence of a gas reservoir close to the AGN (Schmitt, Storchi-Bergmann & Fernandes 1999; Boisson et al. 2000; Storchi-Bergmann et al. 2000; Cid Fernandes et al. 2001, 2005; Storchi-Bergmann et al. 2005). Besides the signatures

⋆E-mail: djfaustus@gmail.com

of young stars observed in spectra of AGN, kpc scale kinematic studies (Nelson & Whittle 1995, 1996) have suggested that Seyfert galaxies have lower mean mass-to-light ratios than normal galaxies, which also could be due to a younger near-nuclear stellar population (Oliva et al. 1995, 1999).

The presence of young stars near the nucleus seems also to be the explanation for the results of recent studies investigating the stellar kinematics on scales of hundred of parsecs (García-Lorenzo, Mediavilla & Arribas 1999; Emsellem et al. 2001; Márquez et al. 2003). These studies have found a central drop in the stellar velocity dispersion (hereafter σ-drop) in a few galaxies with Seyfert nuclei. Wozniak et al. (2003) presented simulations showing that a new generation of stars formed at the centre of the galaxy from cold material would create such a drop which would remain visible for hundreds of Myr. Nevertheless, a decrease in σ towards the nucleus has been recently observed also in late-type non-active galaxies Ganda et al. (2006), supporting its link to recent star formation, but not necessarily to nuclear activity in galaxies.

Most studies available in the literature on kinematics of Seyfert galaxies are based on long-slit observations, which are restricted to only one axis of the host galaxies. In order to properly probe the galactic gravitational potential, as well as to investigate the nature and extent of the σ-drops, it is necessary to cover a 2D region, what we have done in the present work using the Integral Field Unit (IFU) of the Gemini Multi-Object Spectrograph (GMOS).

The power of IFU observations to map the large-scale kinematics of galaxies has been evidenced in recent studies (e.g. Ganda et al. 2006). For AGN, only few such studies are available (e.g. Emsellem et al. 2006 for NGC 1068). Most AGN kinematic studies have focused on gas emission lines, as it is much easier to obtain kinematical data from emission lines than from stellar absorption features. Nevertheless, the gas in the nuclear region of AGNs is subject to non-gravitational effects, such as winds and jets, and in order to probe the gravitational potential, it is necessary to measure the stellar kinematics.

In this work, we use the IFU-GMOS to map the stellar kinematics in the inner few hundred parsecs of six of the closest Seyfert galaxies. The combination of the spatial resolution at the galaxies reached by the observations (down to a few tens of parsecs), 2D coverage, stellar kinematics, and a Seyfert sample is unique in the literature.

This paper is organized as follows. In Section 2, we present the criteria used to select the sample and discuss the relevant information for each galaxy. In Section 3 we describe the observations and reductions, in Section 4 we present the methods used to analyse the data and in Section 5 we report and discuss our results. In Section 6 we present a summary of the results and our conclusions.

2 SAMPLE

We chose to map the stellar kinematics using the Ca II triplet absorption feature around 8500 Å (hereafter Ca-T) due to the fact that this spectral region is not much affected by emission lines and the continuum of the active nucleus, and thus clearer measurements of the stellar kinematics can be made.

The sample galaxies were selected as the closest Seyfert galaxies for which previous spectra in the Ca-T region were available in the literature (Nelson & Whittle 1995), so that we could check, in advance, if the absorption features to be used in the stellar kinematic measurements were clearly present in the spectra. In this work, we present the results for six Seyfert galaxies, whose properties are listed in Table 1.

Table 1. Sample galaxies (column 1), morphological/Seyfert type (columns 2/3), adopted spatial scale (column 4) and seeing measured from the acquisition images (columns 5/6).

Galaxy	Morphological type	Seyfert type	Scale (pc/arcsec)	Image quality[a] (arcsec)	(pc)
NGC 2273	SBa	2	120	1.00	120
NGC 3227	SAB pec	1.5	84	0.80	67
NGC 3516	S0	1.5	183	0.98	180
NGC 4051	SABbc	1	45	0.50	23
NGC 4593	SBb	1	174	0.49	85
NGC 4941	Sab	2	72	0.40	29

[a]Although this has been obtained from the PSF measured in the acquisition image, we verified that the nuclear PSF measured in the reconstructed image of the Seyfert 1 galaxies is the same for NGC 4051 and only ~10 per cent larger for NGC 4593.

Besides selecting the galaxies on the basis of their proximity and detectability of the stellar Ca-T, we also looked for the presence of strong [S III] λ9069 line emission, as this line could be included in the same observational set up used to observe the Ca-T. The results based on the measurements of this emission line, such as intensity maps and gaseous kinematics, will be presented in a forthcoming paper.

We have also observed kinematic standard stars, to be used as references in the measurement of the radial velocities and velocity dispersions of the sample galaxies.

2.1 NGC 2273

From a 6 cm radio map, Ulvestad & Wilson (1984) found the nucleus to be resolved into two distinct components separated by 0.9 arcsec along E–W. Ferruit, Wilson & Mulchaey (2000), using *Hubble Space Telescope* (*HST*), resolved the central ovoid of the galaxy, which shows two arc-like structures forming a partial nuclear ring, with semimajor axis of ~2.5 arcsec, observed both in a broad-band and in a [N II]+Hα emission-line image. They suggest that emission in the ring, also weakly observed in [O III], comes from H II regions.

The partial ring is also detected in a colour map log(F547M/ F791W) which presents lower values to NW suggesting this is the near side of the ring. The analysis of the [O III] and [N II]+Hα emission-line images reveals a jet-like structure which extends by 2 arcsec to E of the nucleus and is aligned with the radio structures observed in 6 cm.

Subsequent investigation (Erwin & Sparke 2003) based on *HST* images and colour maps led the authors to classify the nuclear ring as a star-forming ring. They also classified the structure internal to the ring as a luminous two-armed blue spiral in opposition to a previous bar-like interpretation (Mulchaey & Regan 1997).

The large $H - K$ colour index and high 10 μm luminosity, extended by more than 5 arcsec also supports the presence of a circumnuclear starburst (Devereux 1989; Young & Devereux 1991).

2.2 NGC 3227

This galaxy forms an interacting pair with the elliptical galaxy NGC 3226. Gonzalez Delgado & Perez (1997) reported traces of young stellar population in the nuclear optical spectrum. Mundell et al. (1995) studied the H I emission and found that the galaxy disc is inclined by 56° with major axis at position angle (PA) = 158°

and contains an H I mass of $5.7 \times 10^8 \, M_\odot$. H_2 maps have been obtained by Quillen et al. (1999) from *HST*/NICMOS images and show elongated emission along PA $\sim 100°$. Meixner et al. (1990) obtained ^{12}CO (1–0) maps showing a nuclear double peak aligned roughly E–W separated by 2 arcsec and extended emission running from SE to NW at $30°$ from the major axis of the galaxy (the direction pointing to the companion galaxy NGC 3226). To explain these maps Fernandez et al. (1999) proposed a gas 'disc' of 100 pc diameter with a major axis along PA $\sim 100°$. Better resolution ^{12}CO (1–0) and ^{12}CO (2–1) maps were obtained by Schinnerer, Eckart & Tacconi (2000) who find that the central region is resolved into an uneven ring-like structure with radius ~ 3 arcsec and the E part six times brighter than the W part. These maps also show the SE–NW extended structures and a nuclear bar that connects the ring to the external NW component. The kinematical analysis led them to conclude that a warped gas disc provides a better description of the observed gas motions than a bar.

2.3 NGC 3516

This was the first Seyfert galaxy with detected line variability (Andrillat & Souffrin 1968). More recently Weaver, Gelbord & Yaqoob (2001) observed variability in both the X-ray continuum and Kα line. Regan & Mulchaey (1999), using *HST* images showed that a single dust spiral pattern dominates the nuclear morphology. Using *J*-band images Quillen et al. (1999) proposed that this galaxy has two bars. Nagar et al. (1999) found a radio jet along PA $\sim 10°$ which corresponds to the near side of the galaxy, according to Malkan, Gorjian & Tam (1998), so this jet would be projected against the near side of the galaxy. Hα+[N II] and [O III] images show a 'Z'-shaped circumnuclear emission extended by ~ 20 arcsec from SW to NE (Pogge 1989; Miyaji, Wilson & Perez-Fournon 1992). The gas velocities inside this structure cannot be reproduced by rotation, but can be explained by a nuclear outflow (Mulchaey et al. 1992; Veilleux, Tully & Bland-Hawthorn 1993). The galactic disc does not contain H II regions, according to Gonzalez Delgado et al. (1997).

Arribas et al. (1997) presented 2D stellar kinematics over a similar field to ours but with poorer spatial resolution. Details about their data and a comparison to ours are discussed in Section 5.

2.4 NGC 4051

Using [O III] emission-line archival *HST* images, Schmitt & Kinney (1996) found an unresolved nuclear source and a low surface brightness component extending 1.2 arcsec from the nucleus along PA = $100°$, approximately the same orientation as that connecting the two radio components at 6 cm detected by Ulvestad & Wilson (1984), which are separated by 0.4 arcsec. In radio 6 and 20 cm but with a resolution of 1 arcsec Ho & Ulvestad (2001) detected a larger scale component extending to SW and NE from the nucleus. Veilleux (1991) reported blue wings in the forbidden optical emission lines and proposed a model with outflow and obscuring dust. The mid- and far-infrared fluxes have been explained by Rodriguez Espinosa et al. (1996) and Contini & Viegas (1999) as due to hot dust emission. In X-rays Lawrence et al. (1985) found variability on time-scales of hundreds of seconds and Salvati et al. (1993) reported a flux change by a factor of 2 at 2.2 μm in 6 months. Using X-ray maps of the nuclear region Singh (1999) proposed the existence of a component associated with the nuclear activity and other associated with a starburst extended by ~ 40 arcsec.

2.5 NGC 4593

This is a Seyfert 1 galaxy with detected nuclear variability in X-rays by Weaver et al. (2001) and in the optical and infrared by Winkler et al. (1992), Kotilainen, Ward & Williger (1993) and Kotilainen & Ward (1994). The Hα map obtained by Gonzalez Delgado et al. (1997) shows ionized gas in a nuclear halo with radius 2–3 arcsec elongated N to S, and at the border of the halo some patches of emission which they suggest to be a broken starburst ring with minor axis length ~ 5.7 arcsec running S to N. There are a number of H II regions in the spiral arms but none in the large-scale bar (Evans et al. 1996).

2.6 NGC 4941

According to the hard and soft X-rays spectra, Maiolino, Risaliti & Salvati (1999) calculated that the nucleus of this galaxy has a column density of $N_H = 4.5 \times 10^{23} \, cm^{-2}$. Extended [O III] emission (Pogge 1989) shows a halo shape extending up to ~ 10 arcsec from the nucleus while Hα emission is concentrated in H II regions along the spiral arms. Schmitt et al. (2001) found two resolved radio components separated by 15 pc along PA = $335°$.

3 OBSERVATIONS AND REDUCTIONS

The data were obtained in queue mode over three semesters at the Gemini North telescope, using the GMOS IFU. The instrumental set-up for each program is shown in Table 2. The spectral resolution was $R \sim 3000$ [full width at half-maximum (FWHM) ~ 100 km s^{-1}] with a wavelength sampling of 0.692 Å pix^{-1}. The GMOS IFU consists of a hexagonal array of 1000 lenslets which send the light through optical fibres to the spectrograph. The lenslet array samples a field of view (FOV) of 7×5 arcsec^2. The sky is sampled with a field which is displaced by 1 arcmin from the object and has one half of the size of the object field. The centres of contiguous lenses are separated by 0.2 arcsec, which is also the distance between opposite faces of the hexagonal lenses. The effective slit aperture for every lens is, however, 0.31 arcsec.

Each half of the fibres (corresponding to half of the FOV) is aligned to a separate pseudo-slit. The data can be obtained using both slits (full FOV) or one slit (half the FOV, or 3.5×5 arcsec^2) with twice the wavelength coverage. The spectra are projected into an array of three 2048×4608 EEV chips disposed side by side with small gaps in between. The peaks of contiguous spectra are separated by ~ 5 pixel. In two-slit mode each pseudo-slit illuminates one side of the array, and the use of passband filters avoids spectral overlap.

Before the spectral observations, one direct image was obtained for centring purposes, allowing an evaluation of the image quality. This value, measured as the FWHM of the stellar point spread functions (PSFs) in the field, is listed in Table 1.

Data reduction was accomplished using generic IRAF[1] tasks as well as specific tasks developed for GMOS data in the GEMINI.GMOS package. The reduction process comprised trimming, bias subtraction, flat-fielding, cosmic rays cleaning, alignment and interpolation of the data across the chips to recover all the spectra in one frame, extraction of the spectra (the tracing is done using flat spectra),

---

[1] IRAF is distributed by the National Optical Astronomy Observatories, which is operated by the Association of Universities for Research in Astronomy, Inc. (AURA) under cooperative agreement with the National Science Foundation.

Table 2. Details of the observations.

PROGID	Date (MM/YYYY)	Observed galaxies	Field size (arcsec)	Exposure time (s)	Grating/ filter	Spectral coverage (Å)
GN-2002B-Q-15	12/2002	NGC 3227	3.5 × 5	1440	R400/RG610_G0307	6400–10 400
		NGC 3516		1440	R400/RG610_G0307	
		BD +31 22 14				
GN-2003A-Q-20	03/2003	NGC 4051	7 × 5	1800	R400/CaT_G0309	8250–9450
		NGC 4941		1800	R400/CaT_G0309	
		BD +21 24 25				
GN-2004A-Q-1	02/2004	NGC 2273	7 × 5	3600	R400/CaT_G0309	7700–9500
		NGC 4593		3600	R400/CaT_G0309	
		BD +31 22 14				
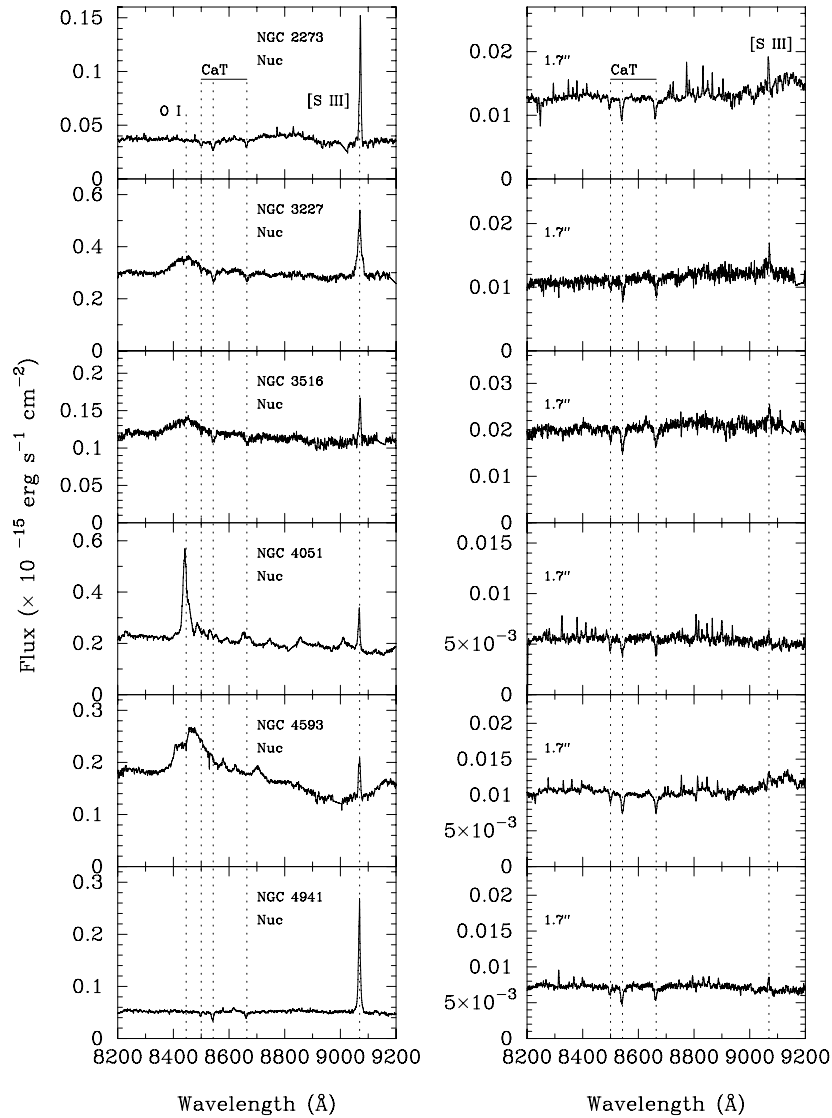
Figure 1. Typical spectra of our sample. In the left-hand panels, we show the nuclear spectra of the lens with the strongest continuum flux (adopted as corresponding to the nucleus) and in the right-hand panels the spectra of a lens displaced 1.7 arcsec towards left-hand side from the centre of the array. Each left–right spectra pair corresponds to the same galaxy and is identified by a label in the left-hand panel. The spectra have been brought to rest frame and the main spectral features are identified by vertical dashed lines.

wavelength calibration, sky subtraction and co-addition of different exposures.

In Fig. 1 we show, for each galaxy, the spectra from selected lenses. The left-hand panels show the nuclear spectra, defined as the one with the strongest flux in the continuum around λ8500. The right-hand panel shows the spectra corresponding to a lens located at 1.7 arcsec from the centre of the array, towards the left-hand side of the IFU field.

The nuclear spectra of the Seyfert 1 galaxies NGC 4051 and 4593 present too much contamination from the AGN continuum and emission lines. In the case of NGC 4051 these lines include the O I blend at λ8446, Ca-T in emission and a number of Paschen emission lines. In the case of NGC 4593 the O I emission is very broad and there are a number of other emission lines (e.g. N I λ8703.2). These strong emission lines precluded the measurements of the stellar kinematics within ∼0.8 arcsec from the nucleus in these galaxies. This effect was unexpected on the basis of the previously inspected integrated spectra (Nelson & Whittle 1995), probably because it was diluted in their large aperture. In any case, the information we could obtain for these galaxies outside the contaminated region is still valuable and have been included in the present work. The spectra of the Seyfert 1.5 galaxies NGC 3227 and 3516 (some authors classify the latter as Sy 1) present weak contamination from the broad O I line which, however, does not affect the measurements significantly, as the two strongest absorption lines of the Ca-T are unaffected.

Even after subtraction of the sky contribution, there remained some sky-line residuals in the extranuclear spectra, observed in Fig. 1. For these lines as well as for the faint emission lines in the nuclear spectra of NGC 4941, we have set the parameters of the xcsao task (used in the velocity dispersion measurements) to interpolate the continuum eliminating all data points with fluxes higher than 1 standard deviation of the average continuum flux within the cross-correlation window. We have checked that this procedure efficiently eliminated the residual emission lines.

4 DATA ANALYSIS

4.1 Velocity measurements: cross-correlation technique

The kinematic measurements were performed by cross-correlating the spectra of individual lenslets with the spectrum of a kinematic standard star observed with the same set-up as the galaxies. The cross-correlation was performed using the task xcsao of the package RVSAO (Kurtz & Mink 1998) in IRAF, over the spectral range 8430–8900 Å which includes the Ca-T features but avoids the noisy regions at the extremes of the spectra. The task uses the method of the quotient of the Fourier transforms applied to the spectra in velocity space and searches for the peak of the cross-correlation function, fitting a quartic function to the data with values above 50 per cent of the peak and giving as outputs the peak velocity and the FWHM of the cross-correlation function.

As the surface brightness of the galaxies decreases towards the borders of the field, in order to improve the signal-to-noise ratio at these locations, we replaced each individual spectrum by the average of itself and the six nearest spectra (which are closer than 0.3 arcsec). This replacement was done for the spectra beyond a radius 1 arcsec from the centroid of the 8500 Å continuum brightness distribution.

In order to obtain the velocity dispersion values from the measured linewidths we have convolved the spectrum of the kinematic standard star with Gaussian curves of known FWHM – where FWHM = 2.35σ, and σ is the velocity dispersion – to create a set of synthetic spectra. We then performed the cross-correlation between these synthetic spectra and that of the kinematic standard, measuring the FWHM of the cross-correlation function as we did for the galaxies. By plotting the measured widths against the known Gaussian widths we obtain a very tight linear relation which is then used to obtain the real FWHM from the measured FWHM for each galaxy. Finally, as the radial velocities are measured relative to the kinematic standard star, the radial velocity obtained for each galaxy was corrected by the observatory motion relative to the local standard of rest and by the standard star radial velocity as determined from the shifts between the measured wavelengths of the Ca-T lines in the standard spectrum and their rest wavelengths.

4.2 Error calculation

The IRAF cross-correlation task xcsao calculates the error following the method of Tonry & Davis (1979), which is similar to that used by Nelson & Whittle (1995). This method uses the signal-to-noise ratio R and the FWHM w of the cross-correlation peak, assuming that the error in σ is the same as in V_r:

$$\text{error} = \Delta\sigma = \Delta V_r \simeq \frac{3w}{8(1+R)}. \tag{1}$$

For the spectra where the Ca-T lines are clearly detected and are not contaminated by emission lines, we obtain errors in the range 4–17 km s^{-1} for all galaxies. However, there is a loose correlation between the velocity dispersion measurements and the error calculated by this formula, due to a dependence in w that is not fully cancelled by $(1+R)$, an effect also pointed out by Nelson & Whittle (1995). This led us to adopt a conservative approach regarding the error reported by the xcsao task. After inspecting some representative spectra and the calculated error values, we adopted 15 km s^{-1} as the errors in our individual measurements for V_r and σ. We note that this is actually an upper limit, which may overestimates the actual errors for some of the measurements, in particular the ones from the more central spectra.

4.3 Alternative velocity measurements: pixel fitting technique

In order to investigate the dependence of the velocity fields and in particular of the velocity dispersions σ on the measurement technique we have also carried out a kinematic analysis in pixel space (Barth, Ho & Sargent 2002; Cappellari & Emsellem 2004).

Our implementation of the direct-fitting method is essentially the one used in García-Rissmann et al. (2005), the only difference being that we rectified all spectra to account for the different slopes of stellar and galaxy spectra.

We have compared our cross-correlation results with results obtained with this method. We find that the radial velocity measurements are essentially unaltered. We also find that the patterns in the velocity dispersion maps remain the same. We do find a systematic difference in the velocity dispersion values obtained from the two methods but this difference varies from galaxy to galaxy. For example, for NGC 4051 there is no difference at all while for NGC 2273 we find the largest difference. This is illustrated in Fig. 2, where we compare the σ maps obtained with both techniques for NGC 2273. Note that the low dispersion ring (see discussion in Section 5.1) is clearly present in both maps, the only difference being that the values obtained with the direct pixel fitting method are larger by ∼20–30 km s^{-1}.

In order to investigate if this difference could be due to a template mismatch, we have performed velocity dispersion measurements using both techniques and a set of 28 stellar templates from the atlas of Cenarro et al. (2001). The stars were chosen to span a wide range of spectral types. For the cross-correlation technique the results did not vary much for template spectral types G, K and M. Nevertheless, as we moved to earlier spectral types the results began to vary but by simple visual inspection of these template spectra we verified that they are bad matches to the galaxy spectra. In the case of the direct pixel fitting method we made two tests. First we modelled each spectrum with a combination of all 28 templates, letting
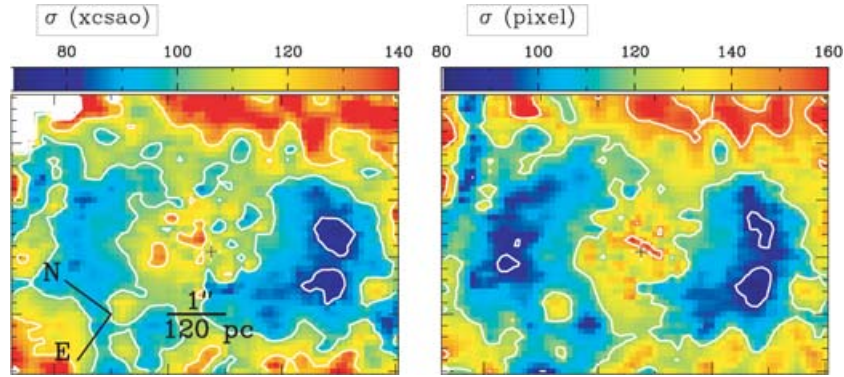
Figure 2. Comparison of σ maps obtained with different methods for NGC 2273. The map on the left-hand panel was obtained using the cross-correlation method, the one on the right-hand panel was obtained using a pixel space fitting technique. In both cases we obtain the same main structure: a low-σ partial ring at ≈ 2 arcsec from the nucleus.

their proportions vary freely, thus accounting for variations in stellar populations (García-Rissmann et al. 2005). Then we repeated the fit using only our observed template star. The difference is negligible (at most a few km s^{-1}), demonstrating that our kinematic measurements are not seriously affected by template mismatch.

4.4 Modelling of the radial velocity field

The radial velocity maps obtained from the measurements described above (see Figs 3–8) show that a clear rotation pattern dominates the stellar kinematics. In order to obtain an analytical description of the radial velocity field, we have adopted a very simple approximation, assuming plane Keplerian orbits for the stars, and representing the gravitational potential of the bulge by a Plummer potential:

$$\Phi = -\frac{GM}{\sqrt{r^2 + a^2}}, \tag{2}$$

which depends only on the scalelength a and bulge mass M, and where r is the radial distance in the plane of the galaxy.

We assume that the stars are in orbits close to a plane $P(i, \psi_0)$ characterized by its inclination relative to the plane of the sky (i) and the PA of the line of nodes ψ_0. Although we do not expect that this simple approximation provides a robust determination of the bulge mass, inclination and bulge scalelength, we can obtain reliable determination of the systemic velocity V_s, PA of the line of nodes ψ_0 and the position of the kinematical centre.

Using the above potential, we calculate the rotation curve in the plane $P(i, \psi_0)$ with coordinates of the origin (X_0, Y_0). The 2D rotation curve is then projected on to the plane of the sky where the radial variable is now R, the angular variable is ψ and the correspondent scalelength is A. The relations between r and R, and between a and A are: $r = \alpha R$ and $a = \alpha A$, where $\alpha = \sqrt{\cos^2(\psi - \psi_0) + \sin^2(\psi - \psi_0)/\cos^2(i)}$. The systemic velocity V_s is added to the model as a zero-point offset.

In summary, there are seven free parameters to be determined by fitting the non-linear model

$$V_r = V_s + \sqrt{\frac{R^2 \, GM}{(R^2 + A^2)^{3/2}}}$$
$$\times \frac{\sin(i)\cos(\psi - \psi_0)}{[\cos^2(\psi - \psi_0) + \sin^2(\psi - \psi_0)/\cos^2(i)]^{3/4}} \tag{3}$$

to the data V_r, what has been done using a Levenberg–Marquardt algorithm.

Before performing the fits, we have inspected the map of uncertainties in radial velocity generated by the cross-correlation routine, the individual spectra and the radial velocity maps in order to obtain an uncertainty threshold to discriminate between reliable data (or measurement) and noise. This threshold varied somewhat from galaxy to galaxy, ranging from 9 to 17 km s^{-1}. Only reliable measurements were used in the data analysis and model fitting. The measurements considered unreliable have been masked in the velocity maps shown in Figs 3–8.

The parameters obtained from the fits are shown in Table 3. The kinematical centre (X_0, Y_0) was used to calculate $\Delta X_0 = X_0 - X_0^b$ and $\Delta Y_0 = Y_0 - Y_0^b$ where X_0^b and Y_0^b are the coordinates of the centroid of the continuum brightness distribution.

5 RESULTS

In this section, we present and discuss the kinematic measurements obtained from the spectra as well as the results of the modelling.

2D maps of the measurements, together with the acquisition image and residuals of the model fits for each galaxy, are presented in Figs 3–8. Each figure comprises six panels, as described below.
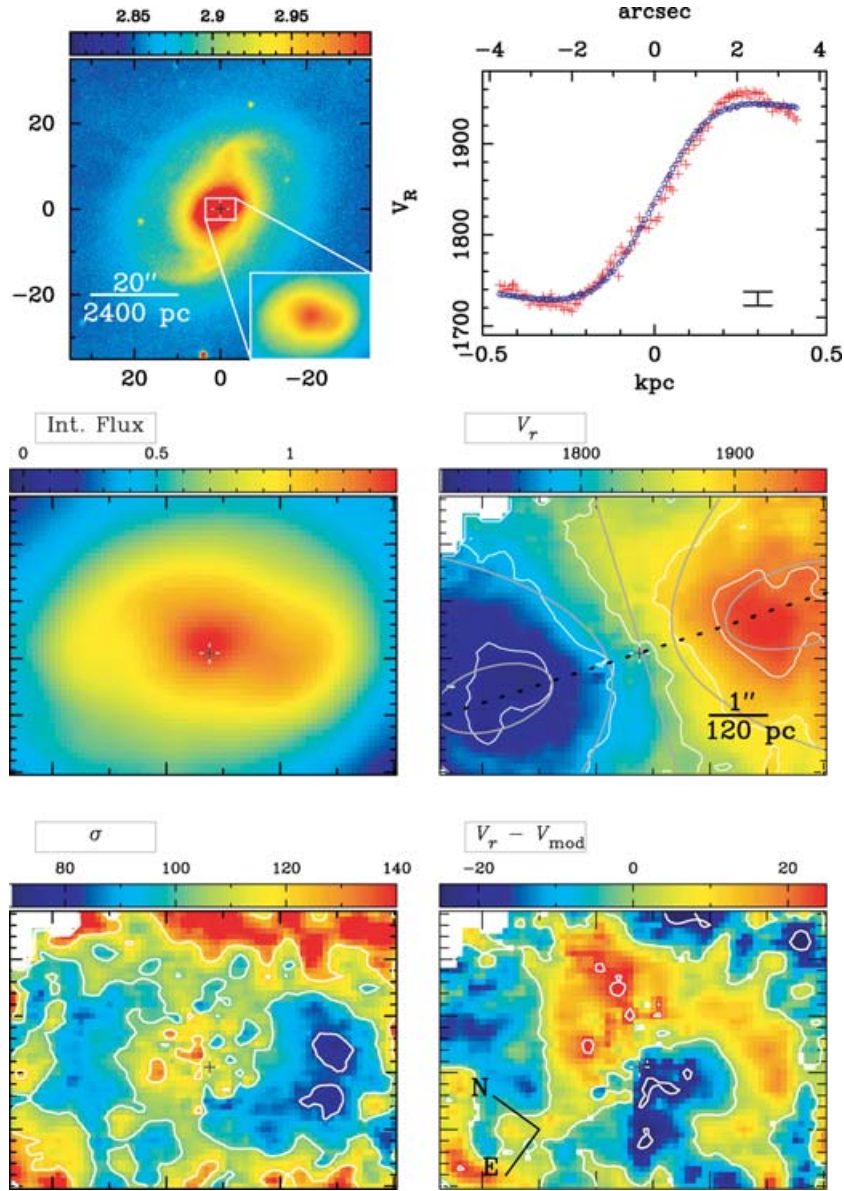
(i) The top left-hand panel shows a large-scale *I*-band image with the IFU field drawn as a white box and the peak of the brightness distribution marked by the black cross. The small inset at the lower right-hand corner details the morphology of the nuclear region covered by the IFU field.

(ii) The top right-hand panel shows the measured radial velocities V_R (red crosses) along a virtual slit placed along the line of nodes and with width 0.6 arcsec, together with the corresponding model values (blue circles), as a function of the projected distance from the nucleus,[2] R. The error bar at the lower right-hand corner represents the maximum uncertainty in the velocity values.

(iii) The remaining panels show 2D maps of measured properties. The middle left-hand panel shows the flux integrated over the wavelength range used in the cross-correlation measurements.

(iv) The middle right-hand panel shows the radial velocity map, with isovelocity contours superimposed; white contours correspond

[2]Note that, due to the fact that the slit width includes more than one lens there may be more than one velocity value for each given radius at the slit, even for the model.

Figure 3. Kinematic data for NGC 2273. The upper left-hand panel shows a large-scale *i′*-band image of the galaxy (spatial units are arcsec) with the IFU field overlaid as a white box and an inset detailing the nuclear region within the FOV of the IFU maps. The central left-hand panel shows the flux integrated over the wavelength range of the cross-correlation measurements. The bottom left-hand panel shows the velocity dispersion map. The upper right-hand panel shows the measured radial velocities from a virtual slit placed along the line of nodes (red), together with the corresponding model values in (blue). The central right-hand panel shows the radial velocity map with isovelocity contours from data and model superimposed (white for the measurements and grey for the model); the cross marks the kinematic centre and the dashed line shows the line of nodes. The bottom left-hand panel shows the velocity dispersion map. The bottom right-hand panel shows the residuals between the measured radial velocities and the model. All panels have the same orientation, indicated at the bottom right-hand panel. The four bottom panels share the scale indicated in the central right-hand panel, and angular extents of 6.8×4.9 arcsec^2. Regions in white correspond to uncertain measurements which have not been included in the fits.

to the measurements, while grey contours correspond to the best-fitting model. The kinematic centre is identified by the black cross, and the line of nodes is indicated by the black dashed line.

(v) The bottom left-hand panel shows the velocity dispersion σ map.

(vi) The bottom right-hand panel shows the residuals obtained from the subtraction of the kinematic model from the radial velocity map of panel (iii).

For display purposes, the kinematic maps of Figs 3–8 have been interpolated over the original hexagonal array to generate a rectan-

gular grid uniformly sampled, with pixel size 0.1×0.1 arcsec^2. The scale (shown in panel iii) and orientation (shown in panel v) are the same for all the maps for a given galaxy.

Table 4 lists the velocity dispersions measured from the integrated nuclear spectra inside circular[3] apertures with diameters 0.6 and 1 arcsec for those galaxies with reliable nuclear data, as discussed in Section 3. Comparing our values with those from Nelson & Whittle (1995), we conclude that they are compatible given the uncertainties

---

[3]Actually the combined spectra from all hexagonal elements with centres within the circular aperture radii.
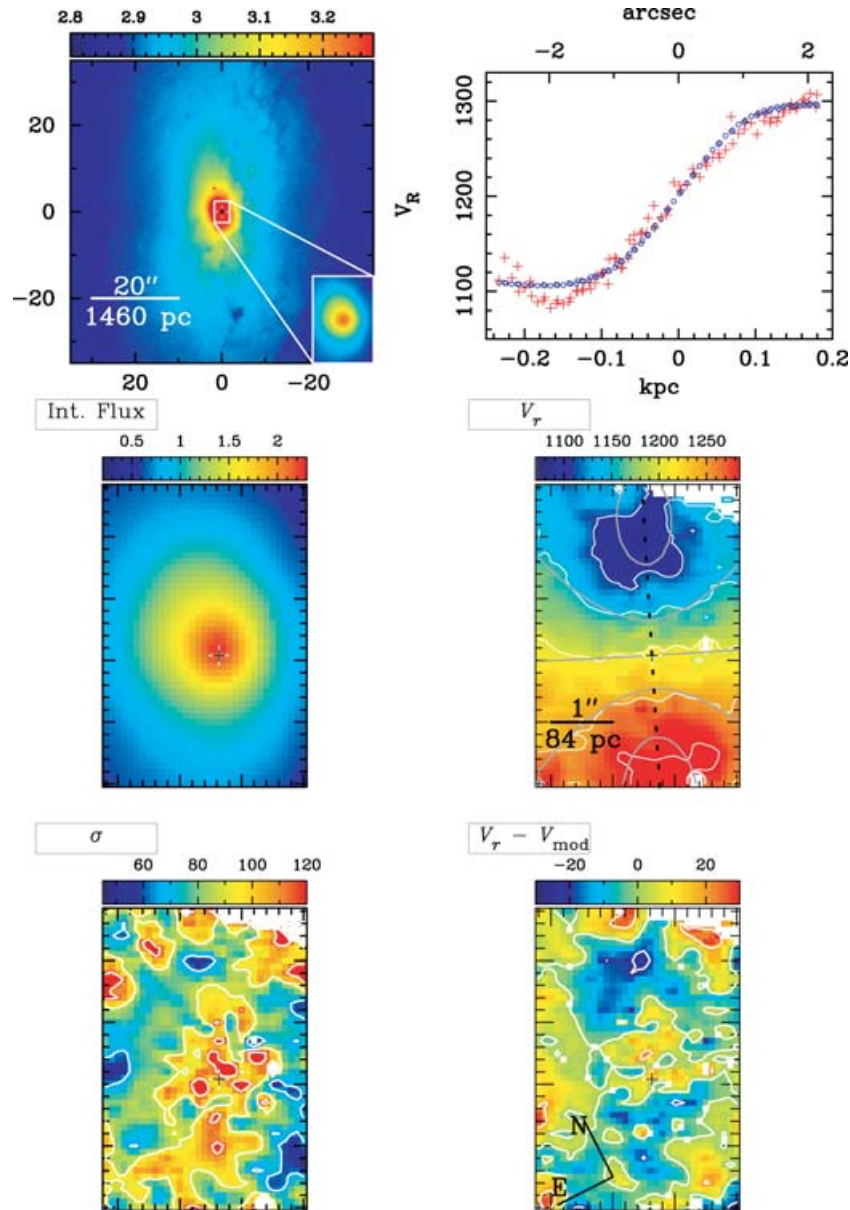
Figure 4. Kinematic data for NGC 3227. Details are as described in the caption of Fig. 3, except for the fact that the IFU field is half the size, or 3.3 × 4.9 arcsec^2.

and our smaller apertures. The value given by Terlevich, Diaz & Terlevich (1990) for NGC 3516 is significantly larger than ours, but these authors also present higher values than those of Nelson & Whittle (1995) for other galaxies in common. For NGC 4051 and 4593 the central velocity dispersions are unreliable due to the strong contribution from the AGN continuum.

We now discuss the results obtained for each galaxy.

5.1 NGC 2273

The radial velocity map (central right-hand panel of Fig. 3) shows a rotation pattern which deviates from the classical spider diagram, evidenced by the fact that the observed kinematic minor and major axes are not perpendicular to each other, indicating deviations from axial symmetry. The residuals map show indeed deviations from the model above the noise level, which seem to be co-spatial with the star-forming ring (see discussion below).

The rotation curve (upper right-hand panel of Fig. 3) along the kinematic major axis seems to have reached the turnover at only 250 pc from the nucleus. In addition, the data turnover seems to be more pronounced than that of the model, suggesting a more concentrated mass distribution.

The velocity dispersion map (bottom left-hand panel of Fig. 3) presents a ring-like structure with values of about 60–80 km s^{-1} while in the centre the velocity dispersion reaches values of up to 100 km s^{-1}. In Fig. 9 we present 1D cuts of the velocity dispersion map along the major and minor axis of the galaxy which helps the visualization of the ring-like structure. This structure is co-spatial with the nuclear partial ring observed in the *HST* line emission images and colour maps of Ferruit et al. (2000). The lower velocity dispersion can be interpreted as a signature of recently formed stars, which still keep – at least partially – the kinematics of the gas from which they have been formed (Wozniak et al. 2003) and thus map the location of a starburst ring with semimajor axis of ∼300 pc. This
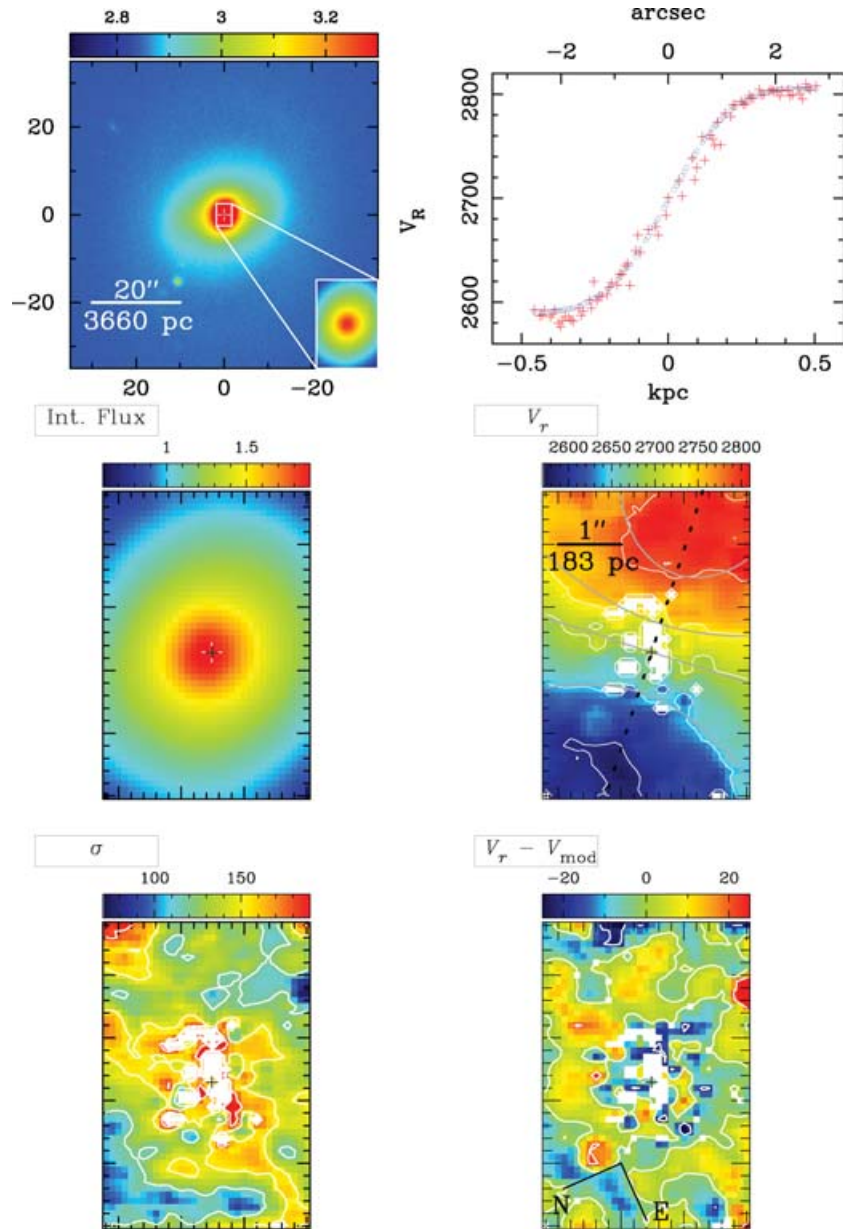
Figure 5. Kinematic data for NGC 3516. Details are as described in the caption of Fig. 3, except for the fact that the IFU field is half the size, or 3.3 × 4.9 arcsec^2.

interpretation is supported by the recent study of Allard, Peletier & Knapen (2005), which shows a similar circumnuclear ring of low gas velocity dispersion associated with ongoing star formation.

5.2 NGC 3227

Our radial velocity map (central right-hand panel of Fig. 4) also shows a rotation pattern, where the redshifted side is to SE of the nucleus, in agreement with the H I radial velocity data of Schinnerer et al. (2000). The line of nodes PA obtained from the model (=156°.7) agrees within 4° with the values found by Mundell et al. (1995) and Schinnerer et al. (2000).

The residuals of the model fitting, shown in the bottom right-hand panel of Fig. 4, are mostly below ±15 km s^{-1}, except for two blueshifted regions approximately along the line of nodes, which deviate from the model by more than 20 km s^{-1}. The rotation curve

(upper right-hand panel) suggests that to NW the turnover has been reached already at ∼150 pc from the nucleus, while this does not happen to the SE.

The velocity dispersion map (bottom left-hand panel of Fig. 4) is characterized by a nuclear region with σ above 100 km s^{-1} which drops in all directions but towards SE reaching values of ≈75 km s^{-1} or less. The σ values increase again towards E, N and NW as evidenced in Fig. 10 by two 1D cuts of the σ map. The loci of low-σ regions have a good correspondence to the loci of high CO emission reported by Schinnerer et al. (2000) and referred to as a gas ring. In particular, the loci with the lowest velocity dispersions correspond to those with highest CO emission. The loci of low σ is also co-incident with a ring of blue $J - K$ colour reported by Chapman, Morris & Walker (2000). Although our FOV seems to be too small to clearly reveal the rise of σ beyond the ring in all directions, the coincidence of the low-σ loci with both the CO and $J - K$ rings
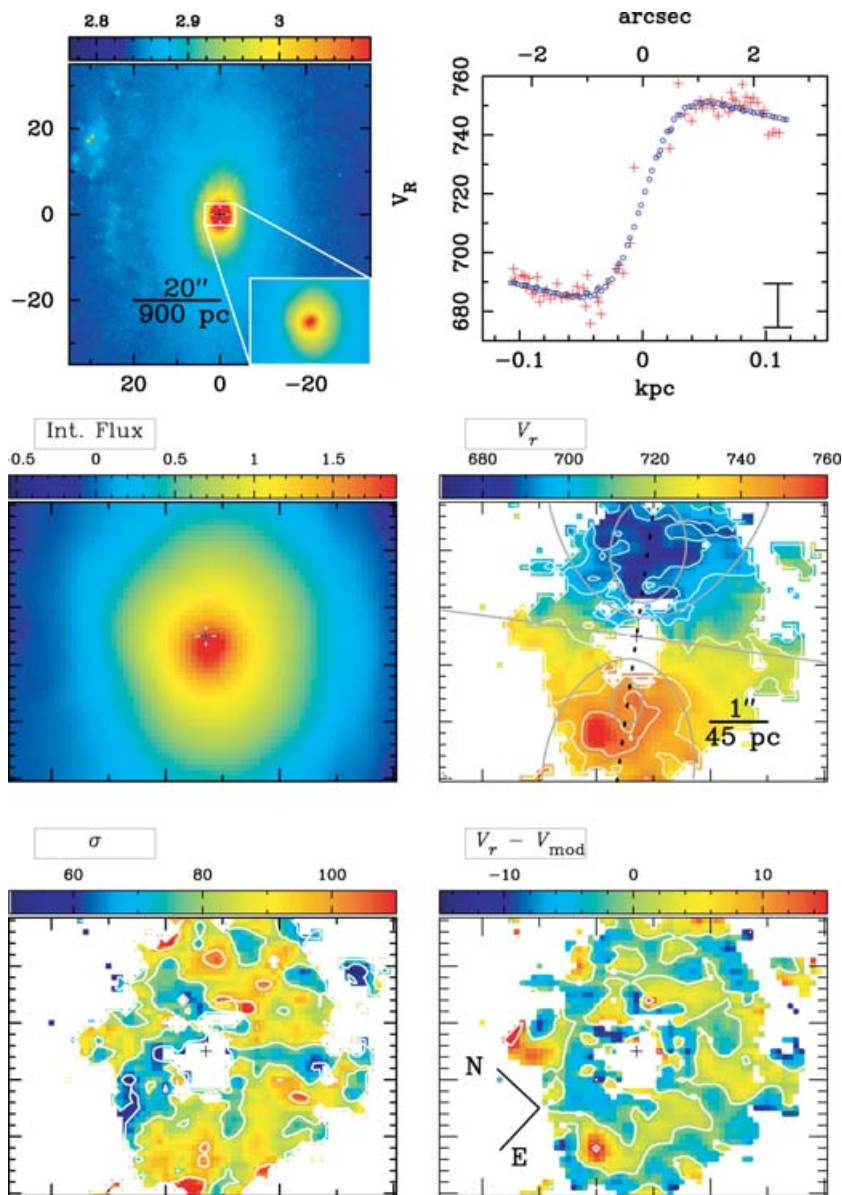
Figure 6. Kinematic data for NGC 4051. Details are as described in the caption of Fig. 3.

supports also the existence of a low-σ ring structure in our data. As in the case of NGC 2273 our interpretation is that we are observing a ring of recent star formation where the low σ of the stars is due to the low velocity dispersion of the cool gas from which they have formed.

5.3 NGC 3516

The radial velocity map (central right-hand panel of Fig. 5) shows a rotation pattern which seems to reach the turnover at the edge of the field, corresponding to a distance of 500 pc from the nucleus, as can be also seen in the rotation curve (top right-hand panel of Fig. 5). The velocity field is in good agreement with the 2D velocity map of Arribas et al. (1997). The kinematic major axis orientation of $\Psi_0 = 48°.4$ also agree with the values found by these authors. The above value for Ψ_0 is also the orientation of the photometric major axis obtained by fitting ellipses to the most external isophotes in the

i'-band acquisition image (corresponding to an ellipse of semimajor axis 49 arcsec).

From the rotation curve in the top right-hand panel of Fig. 5 we obtain a peak-to-peak amplitude in the velocity field of $\sim$220 km s^{-1}, significantly larger than the one measured by Arribas et al. (1997) (160 km s^{-1}). This discrepancy can be understood if we recall that those authors applied a 1.5 arcsec smoothing to the data, which would flatten the rotation curve. We note that the peak-to-peak amplitude of the stellar rotation is well below the one obtained from the gas kinematics (592 km s^{-1}), by Mulchaey et al. (1992).

Our velocity dispersion map (bottom left-hand panel of Fig. 5) shows typical values in the central region larger than 150 km s^{-1} surrounded by a region with lower σ (as low as $\sim$90 km s^{-1}). From measurements of the Mg I b absorption band, Arribas et al. (1997) reported a central σ of 164 $\pm$ 35 km s^{-1} (within an aperture of 3 arcsec), which is consistent with our data, but a 2D distribution of linewidths does not show any clear structure. In our data we can see
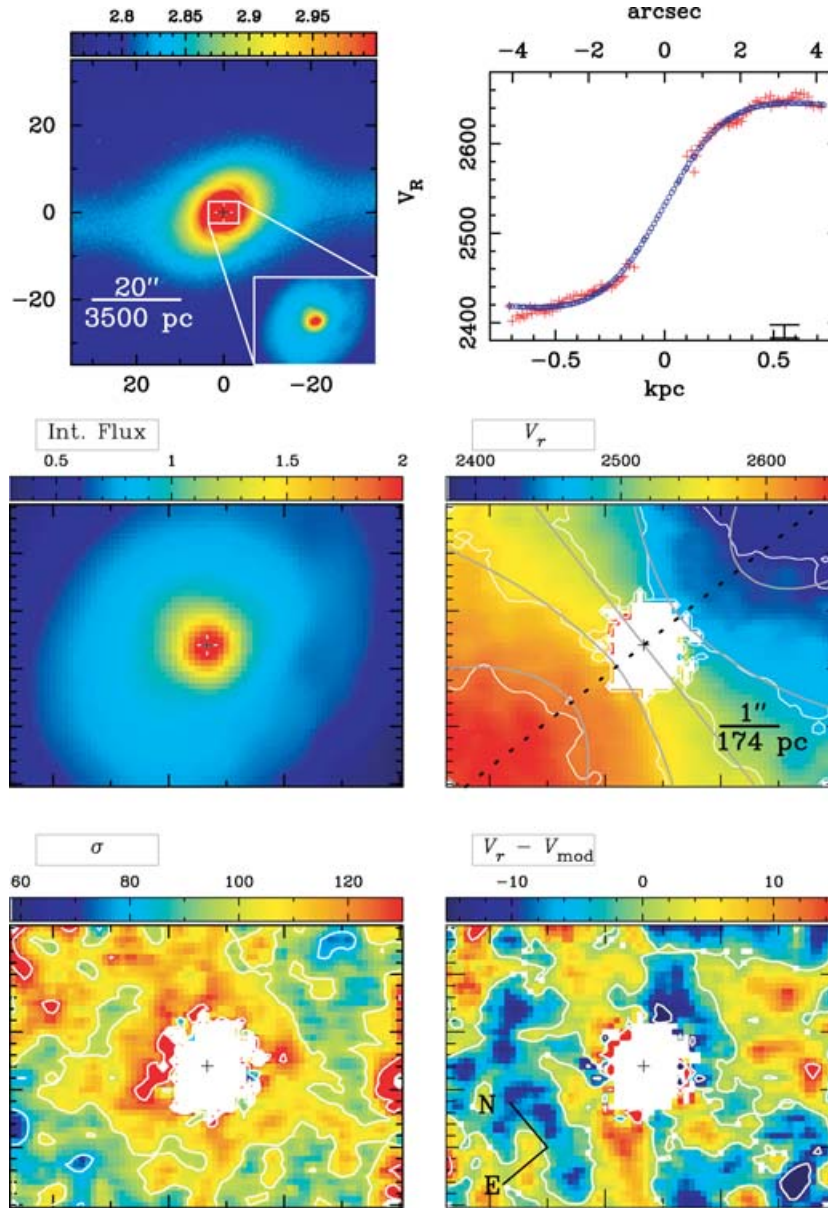
Figure 7. Kinematic data for NGC 4593. Details are as described in the caption of Fig. 3.

lower σ values at locations surrounding the kinematic major axis direction at an average distance from the nucleus of ~400 pc.

The residuals from the radial velocity fit (bottom right-hand panel of Fig. 5) are mostly within the adopted error of ± 15 km s^{-1}.

5.4 NGC 4051

In this galaxy the nuclear continuum and broad Ca-T emission lines preclude reliable measurements of the stellar kinematics using the Ca-T absorption lines within 0.5 arcsec from the nucleus. This region has thus been masked for the model fitting.

The radial velocity map (central right-hand panel of Fig. 6) is dominated by the typical rotation pattern observed in all galaxies so far. The rotation curve (upper right-hand panel of Fig. 6) has a peak-to-peak amplitude of only 130 km s^{-1} for an inclination of the galaxy $i \sim 41°$ (assuming $i = \cos^{-1} b/a$ where a and b are the ma-

jor and minor axis photometric lengths obtained from NASA/IPAC Extragalactic Database) and the turnover seems to occur very close to the nucleus, at $R \sim 50$ pc.

The residuals from the model fit are within the ± 10 km s^{-1} error limits (bottom right-hand panel of Fig. 6) and do not show any well defined structure.

The velocity dispersion map (bottom left-hand panel of Fig. 6), is also irregular with σ values ranging from a minimum of ~60 km s^{-1} to a maximum of ~100 km s^{-1}. Nevertheless, it was not possible to extend the measurements closer to the nucleus than ~0.5 arcsec, making it difficult to draw any conclusion on the σ distribution.

5.5 NGC 4593

For this galaxy, as for NGC 4051, the continuum from the Seyfert nucleus precludes reliable measurements of the stellar kinematics in the central region.
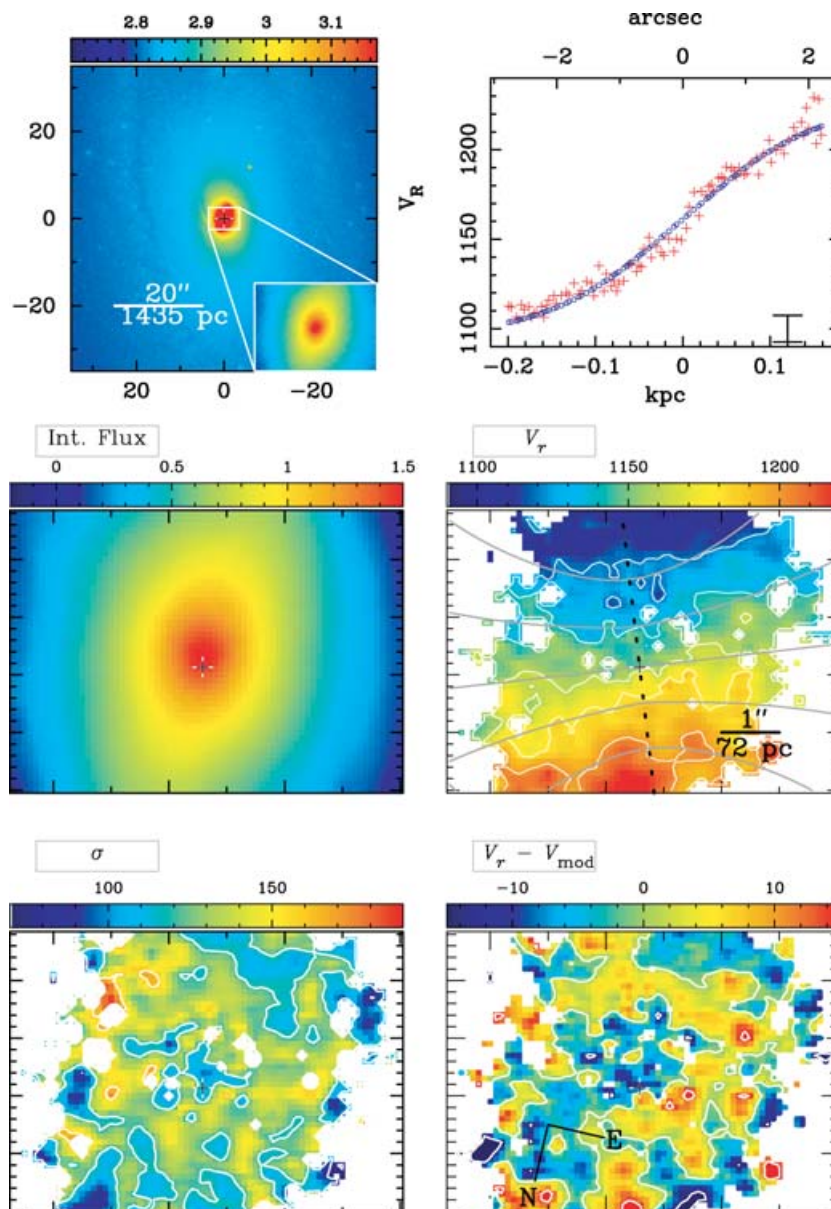
Figure 8. Kinematic data for NGC 4941. Details are as described in the caption of Fig. 3.

The radial velocity map (central right-hand panel of Fig. 7) shows a clear rotation pattern in which the kinematical major axis runs approximately along E–W with the redshifted side to the E.

The peak-to-peak amplitude of the velocity field is 255 km s^{-1}, but the rotation curve (top right-hand panel of Fig. 7) suggests that the maximum velocity may occur beyond the edges of the observed FOV, which corresponds to ∼700 pc from the nucleus along the kinematic major axis.

The velocity dispersion map (bottom left-hand panel of Fig. 7) hints on a rise of the observed values towards the nucleus. At the most central but usable region we find values as high as 120 km s^{-1}. At ∼2.5 arcsec from the nucleus (∼400 pc), the measured values drop to 80–90 km s^{-1}, most notably along the kinematic major axis as in the case of NGC 3516. In the directions approximately perpendicular to the above the velocity dispersion is found to decrease slower, then rise again, reaching up to 130 km s^{-1} at the edges of the field. The map thus hints at the presence of a partial ring structure also for this galaxy. This is supported by the 1D cuts along the major and minor axis of the velocity dispersion map shown in Fig. 11. Alternatively, this region of low-σ values can be associated with a tightly wound spiral arm which can be observed in an *HST* F547M image from Malkan et al. (1998).

Gonzalez Delgado et al. (1997) have reported the presence of a broken starburst ring in an Hα narrow band imaging. But a comparison of our data with theirs shows that our low-σ partial ring is nevertheless internal to their Hα ring.

The radial velocity residuals (bottom right-hand panel of Fig. 7) are within the ±15 km s^{-1} error limits, but show some resemblance to the σ map, suggesting systematic departures from circular rotation in association with the apparent partial ring of lower velocity dispersion.

Table 3. Parameters derived from our modelling.

Galaxy	V_s [a] (km s^{-1})	Ψ_0 (°)	ΔX_0 [b] (pc)	ΔY_0 [b] (pc)	M ($\times 10^9$ M$_\odot$)	A (kpc)	i (°)
NGC 2273	1836	233.4	-7 ± 12	-20 ± 12	2.4	0.17	51
NGC 3227	1201	149.7	-2 ± 9	-10 ± 9	1.4	0.11	43
NGC 3516	2698	48.4	-18 ± 18	9 ± 18	15	0.28	22
NGC 4051	718	106.5	4 ± 5	8 ± 5	0.084	0.031	31
NGC 4593	2531	88.5	1 ± 17	4 ± 17	18	0.41	25
NGC 4941	1161	-0.2	1 ± 7	-14 ± 7	3.6	0.24	24

[a]The upper limit for the error in V_s is about 15 km s^{-1}.
[b]ΔX_0 and ΔY_0 are measured relative to the continuum centroid (see text).

Table 4. Comparison between our σ measurements and those from the literature for the central spectra. Columns 2 and 3 present our measurements (see text); columns 4 and 5 present the values from the literature and corresponding apertures. The upper limit for the error in σ is ± 15 km s^{-1}.

|	σ (0.6 arcsec) (km s^{-1})	σ (1 arcsec) (km s^{-1})	σ (NW95) (km s^{-1})	Aperture (arcsec)
NGC 2273	104	105	136 ± 22	1.5×1.4
NGC 3227	114	109	128 ± 13	1.5×2.1
NGC 3516	192	178	235[a]	2.1
NGC 4051		85[b]	88 ± 13	1.5×2.1
NGC 4593		105[b]	124 ± 28	1.5×3.5
NGC 4941	138	136	109 ± 13	1.5×2.1

[a]From Terlevich et al. (1990).
[b]These values were obtained by inspection of the region around the contaminated central portion of the maps. See Section 3 for details.
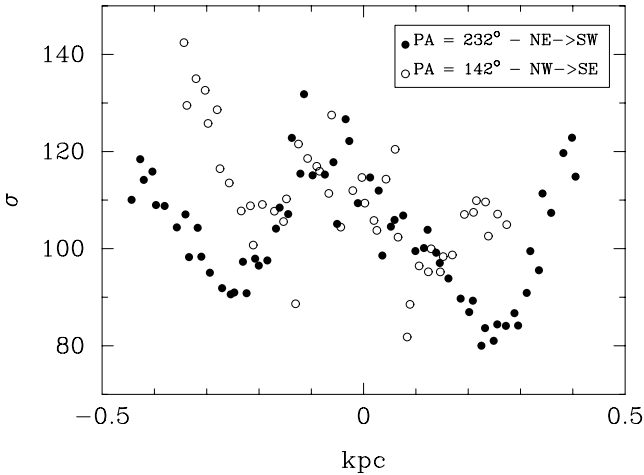
Figure 9. 1D cuts of the 2D σ map of NGC 2273 within pseudo slits 0.3 arcsec wide crossing the nucleus at PAs 232° and 142°.

5.6 NGC 4941

A rotation pattern is again observed in the stellar kinematics (central right-hand panel of Fig. 8). The rotation curve (top right-hand panel of Fig. 8) indicates that the maximum amplitude is located beyond the observed region, which corresponds to a radial distance from the nucleus of only 200 pc for this galaxy.

The velocity dispersion map (bottom left-hand panel of Fig. 8) is almost flat within ∼100 pc from the nucleus, with central values ∼135 km s^{-1}, decreasing to ∼100 km s^{-1} at the edges of the field (∼200 pc).
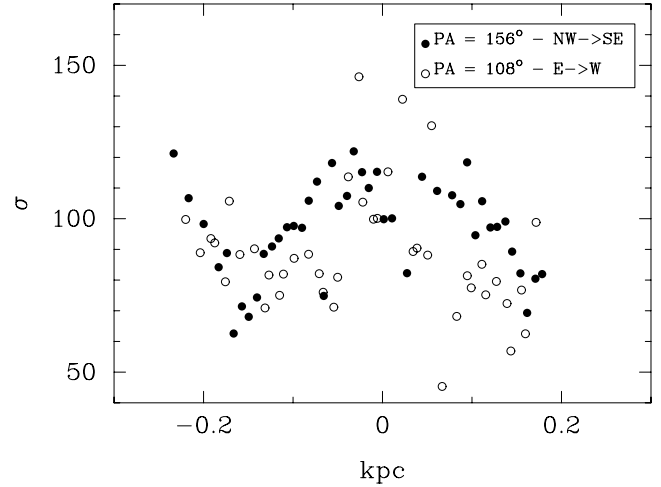
Figure 10. 1D cuts of the 2D σ map of NGC 3227 within pseudo slits 0.3 arcsec wide crossing the nucleus at PA = 156° and 108°.
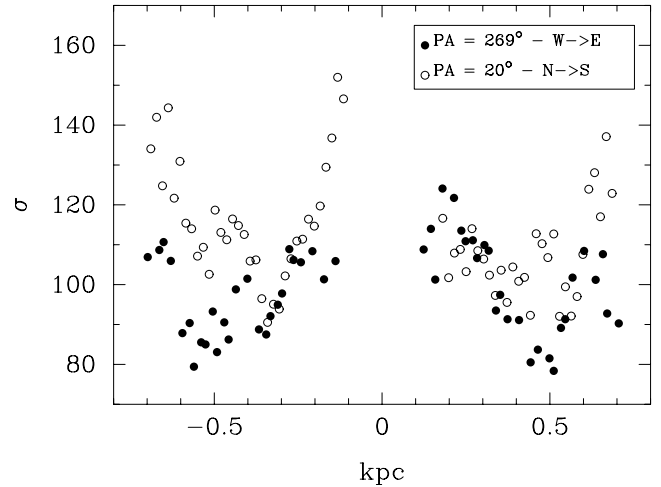
Figure 11. 1D cuts of the 2D σ map of NGC 4593 within pseudo slits 0.3 arcsec wide crossing the nucleus at PA = 269° and 20°.

The radial velocity residuals (bottom right-hand panel of Fig. 8) are within the ± 15 km s^{-1} error limit and show no obvious pattern.

6 SUMMARY AND CONCLUSIONS

In this work, we have obtained 2D maps of the stellar kinematics of the inner few hundred parsecs of six nearby Seyfert galaxies at sub-

arcsecond angular resolution, corresponding to spatial resolutions ranging from 30 to 180 pc at the galaxies.

The stellar velocity field is dominated by rotation, well represented by a simple model where the stars follow plane circular orbits under a Plummer potential. The residuals between measured and modelled radial velocities are always smaller than ± 25 km s^{-1}.

In most cases, the turnover of the rotation curve seems to occur within or close to the edges of the observed field, at radial distances ranging from $\sim$50 pc for NGC 4051 to $\sim$500–700 pc for NGC 3516 and 4593. Only for NGC 4941, for which our observations reach only as far as $\approx$200 pc from the nucleus, the turnover was not observed within the IFU FOV.

The case of NGC 4051 is particularly interesting because the turnover is at only $\sim$50 pc from the nucleus, suggesting that the stellar motions are dominated by a highly concentrated gravitational potential. Indeed, the scalelength of the Plummer potential obtained for this galaxy is the smallest of the sample, $A = 31$ pc. Adopting $\sigma = 85$ km s^{-1} for the nuclear velocity dispersion (the mean value of innermost usable pixels), and the Tremaine et al. (2002) relation, we infer a black hole mass of 4.5×10^6 M$_\odot$, which implies a sphere of influence of only 2.5 pc radius. These values are consistent with those by Peterson et al. (2004), who obtained a black hole mass of 1.9×10^6 M$_\odot$ corresponding to a sphere of influence of 1.2 pc radius. Such concentrated potential is unlikely to be responsible for the small potential-scale size we have found. A more likely interpretation is that the bulge is itself compact and concentrated. Indeed, unlike most Seyferts, this galaxy is late-type (Scd), with a small bulge effective radius.

The velocity dispersion maps are featureless for NGC 4051 and 4941. For the other galaxies the velocity dispersion maps show higher values at the centre and smaller values at 200–400 pc from the nucleus. In the case of NGC 3516 the lowest σ values are observed towards the border of the IFU field, at location close to the kinematic major axis. For NGC 2273, the spatial distribution of lower σ values defines a ring-like morphology which is co-spatial with partial nuclear ring structures seen in line emission images and colour maps of previous works. For NGC 3227, the velocity dispersion map shows a very good correspondence between the region of low-σ values – which seems to delineates a partial ring structure – and regions of high ^{12}CO (2–1) emission and blue $J - K$ colours observed in previous works. A partial ring of low-σ values is also hinted in NGC 4593. As for the nuclear σ-drops found by previous authors (e.g. García-Lorenzo et al. 1999; Emsellem et al. 2001; Márquez et al. 2003) the circumnuclear σ-drops we found in the present study can be interpreted as regions of higher (past or present) gas concentration, harbouring younger stars which still preserve the lower velocity dispersion of the original gas from which they have formed.

REFERENCES

Allard E. L., Peletier R. F., Knapen J. H., 2005, ApJ, 633, L25
Andrillat Y., Souffrin S., 1968, Astrophys. Lett., 1, 111
Arribas S., Mediavilla E., Garcia-Lorenzo B., del Burgo C., 1997, ApJ, 490, 227
Barth A. J., Ho L. C., Sargent W. L. W., 2002, AJ, 124, 2607
Boisson C., Joly M., Moultaka J., Pelat D., Serote Roos M., 2000, A&A, 357, 850
Cappellari M., Emsellem E., 2004, PASP, 116, 138
Cenarro A. J., Cardiel N., Gorgas J., Peletier R. F., Vazdekis A., Prada F., 2001, MNRAS, 326, 959
Chapman S. C., Morris S. L., Walker G. A. H., 2000, MNRAS, 319, 666
Cid Fernandes R., Heckman T., Schmitt H., Delgado R. M. G., Storchi-Bergmann T., 2001, ApJ, 558, 81
Cid Fernandes R., González Delgado R. M., Storchi-Bergmann T., Martins L. P., Schmitt H., 2005, MNRAS, 356, 270
Contini M., Viegas S. M., 1999, ApJ, 523, 114
Devereux N. A., 1989, ApJ, 346, 126
Emsellem E., Greusard D., Combes F., Friedli D., Leon S., Pécontal E., Wozniak H., 2001, A&A, 368, 52
Emsellem E., Fathi K., Wozniak H., Ferruit P., Mundell C. G., Schinnerer E., 2006, MNRAS, 365, 367
Erwin P., Sparke L. S., 2003, ApJS, 146, 299
Evans I. N., Koratkar A. P., Storchi-Bergmann T., Kirkpatrick H., Heckman T. M., Wilson A. S., 1996, ApJS, 105, 93
Fernandez B. R., Holloway A. J., Meaburn J., Pedlar A., Mundell C. G., 1999, MNRAS, 305, 319
Ferrarese L., Merritt D., 2000, ApJ, 539, L9
Ferruit P., Wilson A. S., Mulchaey J., 2000, ApJS, 128, 139
Ganda K., Falcón-Barroso J., Peletier R. F., Cappellari M., Emsellem E., McDermid R. M., Tim de Zeeuw P., Carollo C. M., 2006, MNRAS, 367, 46
García-Lorenzo B., Mediavilla E., Arribas S., 1999, ApJ, 518, 190
Garcia-Rissmann A., Vega L. R., Asari N. V., Cid Fernandes R., Schmitt H., González Delgado R. M., Storchi-Bergmann T., 2005, MNRAS, 359, 765
Gebhardt K. et al., 2000, ApJ, 539, L13
Gonzalez Delgado R. M., Perez E., 1997, MNRAS, 284, 931
Gonzalez Delgado R. M., Perez E., Tadhunter C., Vilchez J. M., Rodriguez-Espinosa J. M., 1997, ApJS, 108, 155
Ho L. C., Ulvestad J. S., 2001, ApJS, 133, 77
Kotilainen J. K., Ward M. J., 1994, MNRAS, 266, 953
Kotilainen J. K., Ward M. J., Williger G. M., 1993, MNRAS, 263, 655
Kurtz M. J., Mink D. J., 1998, PASP, 110, 934
Lawrence A., Watson M. G., Pounds K. A., Elvis M., 1985, MNRAS, 217, 685
Maiolino R., Risaliti G., Salvati M., 1999, A&A, 341, L35
Malkan M. A., Gorjian V., Tam R., 1998, ApJS, 117, 25
Márquez I., Masegosa J., Durret F., González Delgado R. M., Moles M., Maza J., Pérez E., Roth M., 2003, A&A, 409, 459
Meixner M., Puchalsky R., Blitz L., Wright M., Heckman T., 1990, ApJ, 354, 158
Miyaji T., Wilson A. S., Perez-Fournon I., 1992, ApJ, 385, 137
Mulchaey J. S., Regan M. W., 1997, ApJ, 482, L135
Mulchaey J. S., Tsvetanov Z., Wilson A. S., Perez-Fournon I., 1992, ApJ, 394, 91

Mundell C. G., Pedlar A., Axon D. J., Meaburn J., Unger S. W., 1995, MNRAS, 277, 641

Nagar N. M., Wilson A. S., Mulchaey J. S., Gallimore J. F., 1999, ApJS, 120, 209

Nelson C. H., Whittle M., 1995, ApJS, 99, 67

Nelson C. H., Whittle M., 1996, ApJ, 465, 96

Oliva E., Origlia L., Kotilainen J. K., Moorwood A. F. M., 1995, A&A, 301, 55

Oliva E., Origlia L., Maiolino R., Moorwood A. F. M., 1999, A&A, 350, 9

Peterson B. M. et al., 2004, ApJ, 613, 682

Pogge R. W., 1989, ApJS, 71, 433

Quillen A. C., Alonso-Herrero A., Rieke M. J., Rieke G. H., Ruiz M., Kulkarni V., 1999, ApJ, 527, 696

Regan M. W., Mulchaey J. S., 1999, AJ, 117, 2676

Rodriguez Espinosa J. M., Perez Garcia A. M., Lemke D., Meisenheimer K., 1996, A&A, 315, L129

Salvati M. et al., 1993, A&A, 274, 174

Schinnerer E., Eckart A., Tacconi L. J., 2000, ApJ, 533, 826

Schmitt H. R., Kinney A. L., 1996, ApJ, 463, 498

Schmitt H. R., Storchi-Bergmann T., Fernandes R. C., 1999, MNRAS, 303, 173

Schmitt H. R., Ulvestad J. S., Antonucci R. R. J., Kinney A. L., 2001, ApJS, 132, 199

Singh K. P., 1999, MNRAS, 309, 991

Storchi-Bergmann T., Raimann D., Bica E. L. D., Fraquelli H. A., 2000, ApJ, 544, 747

Storchi-Bergmann T., Nemmen R. S., Spinelli P. F., Eracleous M., Wilson A. S., Filippenko A. V., Livio M., 2005, ApJ, 624, L13

Terlevich E., Diaz A. I., Terlevich R., 1990, MNRAS, 242, 271

Tonry J. L., Davis M., 1979, AJ, 84, 1511

Tremaine S. et al., 2002, ApJ, 574, 740

Ulvestad J. S., Wilson A. S., 1984, ApJ, 285, 439

Veilleux S., 1991, ApJS, 75, 383

Veilleux S., Tully R. B., Bland-Hawthorn J., 1993, AJ, 105, 1318

Weaver K. A., Gelbord J., Yaqoob T., 2001, ApJ, 550, 261

Winkler H., Glass I. S., van Wyk F., Marang F., Jones J. H. S., Buckley D. A. H., Sekiguchi K., 1992, MNRAS, 257, 659

Wozniak H., Combes F., Emsellem E., Friedli D., 2003, A&A, 409, 469

Young J. S., Devereux N. A., 1991, ApJ, 373, 414

This paper has been typeset from a TEX/LATEX file prepared by the author.